

Mg–O Bond Enables Fast Sodium-Ion Insertion/Extraction in $\text{Fe}_{0.97}\text{Mg}_{0.03}\text{PO}_4$: Achieving Low Voltage Hysteresis and High-Capacity Cathodes

Mengting Deng⁺,^[a] Yu Yuan⁺,^[a] Yian Wang,^[a] Wenbin Fei,^[a] Zonglin Yang,^[a] Yichao Shi,^[a] Han Chen,^[a] Yulei Sui,^{*[a]} and Ling Wu^{*[a]}

Olivine-type FePO_4 garners significant research interest due to its remarkable sodium storage capacity of 177.70 mAh g^{-1} and an appropriate discharge voltage of 2.8 V. However, existing synthesis methods often require complex processes or toxic raw materials, which hinder its further development. Additionally, significant voltage hysteresis, resulting from volume mismatches during phase transitions in the Na^+ insertion/extraction process, decreases discharge voltage and energy density. To overcome these issues, this study utilizes an environmentally friendly and cost-effective aqueous ion exchange method, incorporating a small amount of Mg^{2+} . The volume effect caused by doping and the stabilizing effect of Mg–O bonds

alleviate the voltage hysteresis phenomenon. Kinetic analysis reveals that Mg doping widens Na^+ transport channels, with $\text{Fe}_{0.97}\text{Mg}_{0.03}\text{PO}_4/\text{C}$ exhibiting the highest Na^+ diffusion. Furthermore, DFT analysis uncovers changes in the band gap and electrostatic field around the MO_6 octahedra, elucidating the improved conductivity and Na^+ kinetic. $\text{Fe}_{0.97}\text{Mg}_{0.03}\text{PO}_4/\text{C}$ demonstrates a satisfactory initial capacity (170.54 mAh g^{-1} at 0.2 C) and excellent rate performance (80.60 mAh g^{-1} at 5 C), maintaining a specific capacity of 86.39 mAh g^{-1} after 300 cycles at a 2 C rate. This study approaches from a new direction and presents a novel strategy for advancing the synthesis and modification of high-performance $\text{FePO}_4/\text{NaFePO}_4$.

Introduction

The arrival of the technological era has increased the demand for enhanced energy utilization efficiency and the sustainable development of green energy.^[1] Currently, large-scale energy storage systems are being integrated with renewable energy sources such as wind and tidal power to improve their availability.^[2] Concurrently, the widespread use of energy storage devices, including power batteries and portable power sources, has accelerated the development and deployment of high-performance lithium battery materials.^[3] Among these, lithium iron phosphate (LiFePO_4) is prevalent in commercial applications due to its high specific capacity and discharge power, making it a crucial cathode material.^[4] However, this trend has also heightened concerns about the sustainability of lithium resources and the challenges associated with the recycling and disposal of used lithium batteries.^[5]

As a metal with chemical properties similar to lithium, sodium exhibits potential for the development of sodium-ion batteries as alternatives to lithium-ion batteries.^[6] Among various sodium-ion cathode materials, phosphate-based polyanion cathode materials demonstrate high operating voltages and excellent thermodynamic stability.^[7] Due to the presence of

transition metal elements such as Fe and Mn in their structure, these materials offer favorable economic and environmental benefits.^[8] Notably, olivine-type FePO_4 , which can be synthesized through the delithiation of LiFePO_4 , exhibits exceptionally high sodium-ion storage capacity (theoretical specific capacity of 177.70 mAh g^{-1}) and an appropriate discharge voltage (approximately 2.8 V vs. Na^+/Na).^[9] This provides an effective solution for recycling LiFePO_4 and alleviating the pressure on lithium resources. The preparation of FePO_4 predominantly utilize three-electrode aqueous electrochemical techniques or employ rare and toxic reagents in organic media.^[10] However, these techniques are generally confined to laboratory settings. Furthermore, during the insertion and extraction of Na^+ in FePO_4 , phase transitions from NaFePO_4 to $\text{Na}_{2/3}\text{FePO}_4$ and subsequently to FePO_4 result in significant volume mismatches, leading to considerable voltage hysteresis between the charge and discharge states.^[11] This markedly reduces the discharge voltage and energy density of the material. Although modifications using Mn substitution have been investigated to enhance overall voltage, the Jahn-Teller effect associated with Mn^{3+} impedes these materials from achieving high-rate performance and cycling stability.^[12] Consequently, this limitation restricts their capacity to efficiently store energy when interfaced with power generation methods characterized by unstable output currents.

This study utilizes an ion exchange method in an aqueous medium and implements modifications to suppress voltage hysteresis.^[13] Specifically, a small amount of Mg^{2+} is doped into the FePO_4 lattice to enhance the material's electrochemical performance by leveraging volumetric effects and the stabilizing influence of the Mg–O bond structure. Density of states and

[a] M. Deng,⁺ Y. Yuan,⁺ Y. Wang, W. Fei, Z. Yang, Y. Shi, H. Chen, Y. Sui, L. Wu
School of Iron and Steel, Soochow University, Suzhou 215000, China
E-mail: suiyulei@suda.edu.cn
lwu@suda.edu.cn

[†] These authors contributed equally to this work.

Supporting information for this article is available on the WWW under
<https://doi.org/10.1002/batt.202500040>

differential charge density analyses are conducted to evaluate the effect of Mg doping on the material's conductivity and Na^+ diffusion. Mg^{2+} doping improves the electronic distribution within the MO_6 framework of the polyanion, reduces the band gap, and diminishes the electrostatic field in the Na^+ channels, thereby facilitating rapid Na^+ diffusion. Consequently, the 0.03 Mg-FP/C sample demonstrates an initial discharge capacity of $170.54 \text{ mAh g}^{-1}$ at 0.2 C, coupled with excellent rate performance, achieving 80.60 mAh g^{-1} at 5 C. After 300 charge-discharge cycles at 2 C, the capacity only decreased to 86.39 mAh g^{-1} . Additionally, the Li^+ (from Li_2SO_4) remaining in the solution after the exchange reaction can be converted into Li_3PO_4 for reuse, ensuring no loss of Li^+ .

Results and Discussion

Figure 1a presents the phase structure information of FePO_4 and $\text{Fe}_{1-x}\text{Mg}_x\text{PO}_4$ samples after Li removal. The X-ray diffraction patterns of all samples align well with standard card #97–029–0338, indicating that a small amount of Mg doping does not impact the complete Li removal from LiFePO_4 .

The magnified image on the right side of Figure 1a reveals that the diffraction peaks for the (200) and (311) crystal planes shift towards lower angles as the level of Mg doping increases, indicating increases in their interplanar spacings. Rietveld refinement using GSAS software was performed to investigate changes in lattice parameters after doping (Figure 1b, S1, and Table S1). The low R_p values for all samples demonstrate the reliability of the fitting results. Mg-doping results in the expansion of the a -axis and c -axis of the crystal lattice, which enhances Na^+ diffusion along the b -axis.^[14] Figure 1c presents a schematic diagram of the crystal cell before and after

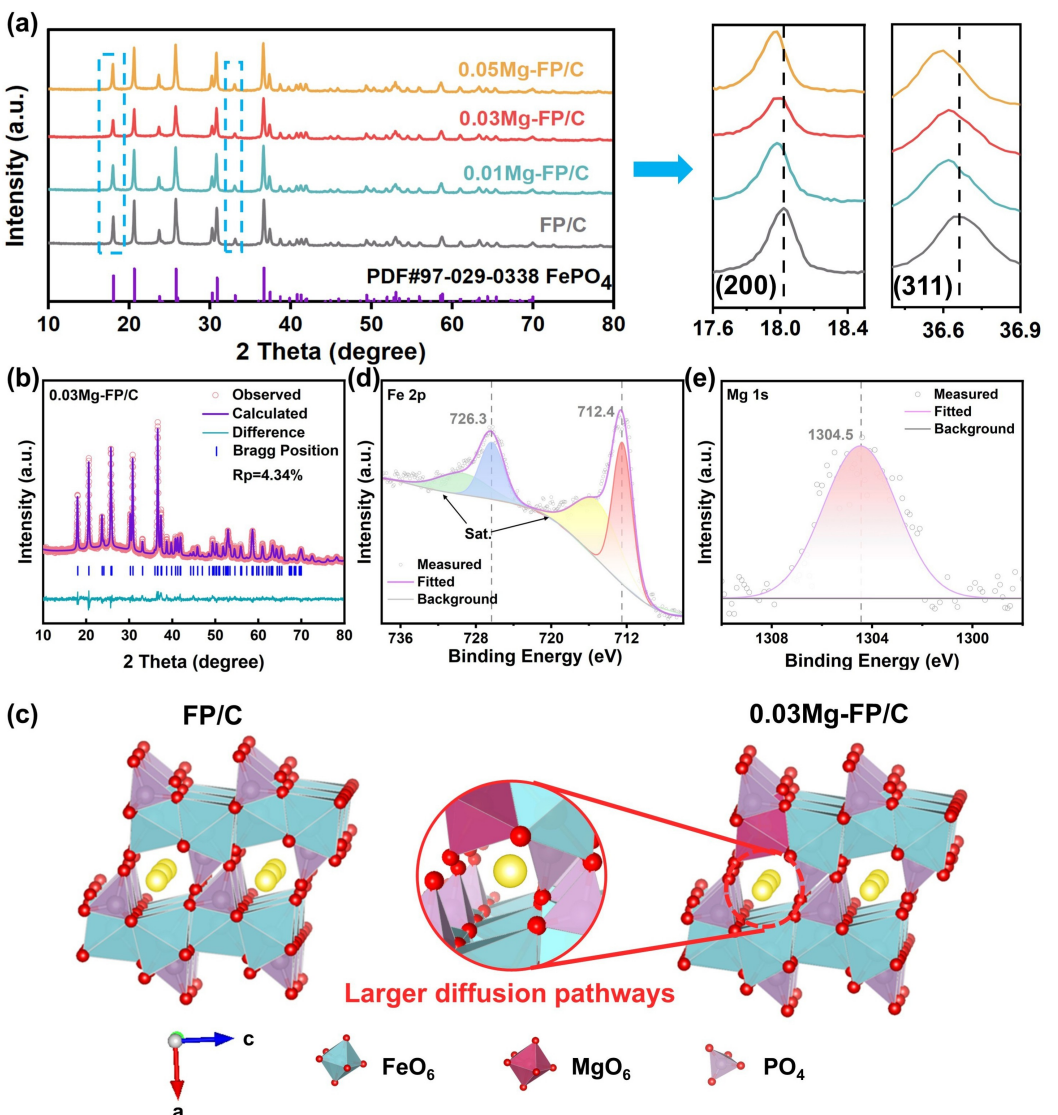


Figure 1. (a) XRD patterns and the local enlargements of samples. (b) Rietveld refinement XRD patterns of 0.03 Mg-FP/C. (c) Crystal structure diagram. The high-resolution XPS spectra of (d) Fe 2p, (e) Mg 1s.

modification. In the MO_6 octahedra, the average Mg–O bond length (2.089 Å) is shorter than the Fe–O bond length (2.149 Å), facilitating greater spatial availability for sodium ion diffusion. In addition, the increase in the average Na–O bond length (from 2.123 Å to 2.129 Å) further indicates that magnesium doping can effectively widen the sodium ion transport channels, thereby enhancing the material's electrochemical performance.^[15] X-ray photoelectron spectroscopy (XPS) was employed to examine the surface chemistry of 0.03 Mg-FP. The XPS survey spectrum in Figure S2 reveals prominent signals for Na, Fe, P, O, and Mg, confirming the presence of these elements. Figure 1d, e illustrate the high-resolution spectra for Fe 2p and Mg 1s. The Fe 2p core-level spectrum exhibits doublet peaks at binding energies of 726.3 eV and 712.4 eV, corresponding to Fe^{3+} 2p_{1/2} and Fe^{3+} 2p_{3/2}, respectively. The Mg 1s core level presents a single peak at a binding energy of 1304.5 eV.^[16] These findings confirm the successful incorporation of Mg^{2+} and the oxidation of Fe^{2+} to Fe^{3+} .

The morphology and elemental distribution of the samples were characterized using SEM and HRTEM. The SEM images (Figure 2a, b, and S3) show that all materials consist of irregularly shaped spheres, with particle agglomeration due to the cross-linking of carbon layers. According to the S–C analysis results (Table S2), the carbon content for FP/C, 0.01 Mg-FP/C, 0.03 Mg-FP/C, and 0.05 Mg-FP/C is 4.93%, 5.04%, 4.96%, and 4.94%, respectively, indicating that Mg-doping does not affect the morphology or carbon content of the materials. The SAED pattern of 0.03 Mg-FP displays distinct lattice spots, demonstrating its excellent crystalline properties, the marked symmetry

points correspond to the (313) crystal plane. As shown in Figure 2d, the primary particle size is approximately 200 nm. In HRTEM images, an amorphous carbon layer about 3 nm thick is observed on the particle surface (Figure 2c), which not only enhances the material's conductivity but also limits excessive crystal growth during the sintering process. In Figure 2f, lattice fringes with a spacing of 0.288 nm are visible, corresponding to the (020) crystal plane. The EDS analysis (Figure 2g) indicates a uniform distribution of Fe, Mg, P, O, and C throughout the material, with no evidence of localized enrichment.

The sodium storage performance of xMg-FP/C was evaluated using cyclic voltammetry (CV) and galvanostatic charge/discharge tests. Figure 3a presents the CV curves of all samples at a scan rate of 0.2 mVs⁻¹. To mitigate the impact of varying active material masses on the comparative results, electrodes with consistent mass were employed for the CV tests. Each curve demonstrates two distinct peaks (A1, A2) during oxidation and a single peak (C1) during reduction, which is due to the two successive stage phase transformations during desodiation, progressing from NaFePO_4 to $\text{Na}_{2/3}\text{FePO}_4$ and subsequently to FePO_4 .^[10a] Notably, 0.03 Mg-FP/C exhibits the highest specific current, suggesting that moderate Mg doping enhances electrochemical reactivity. Figure 3b and c show the first-cycle charge/discharge profiles of all samples at 0.2 C, including their plateau voltages and capacities (capacities within the range of 2.6 V to 2.9 V). The initial discharge capacities for FP/C, 0.01 Mg-FP/C, 0.03 Mg-FP/C, and 0.05 Mg-FP/C were 142.95, 145.98, 170.54, and 165.39 mAh g⁻¹, respectively, demonstrating that Mg doping significantly enhances capacity. In contrast to FP/C, which

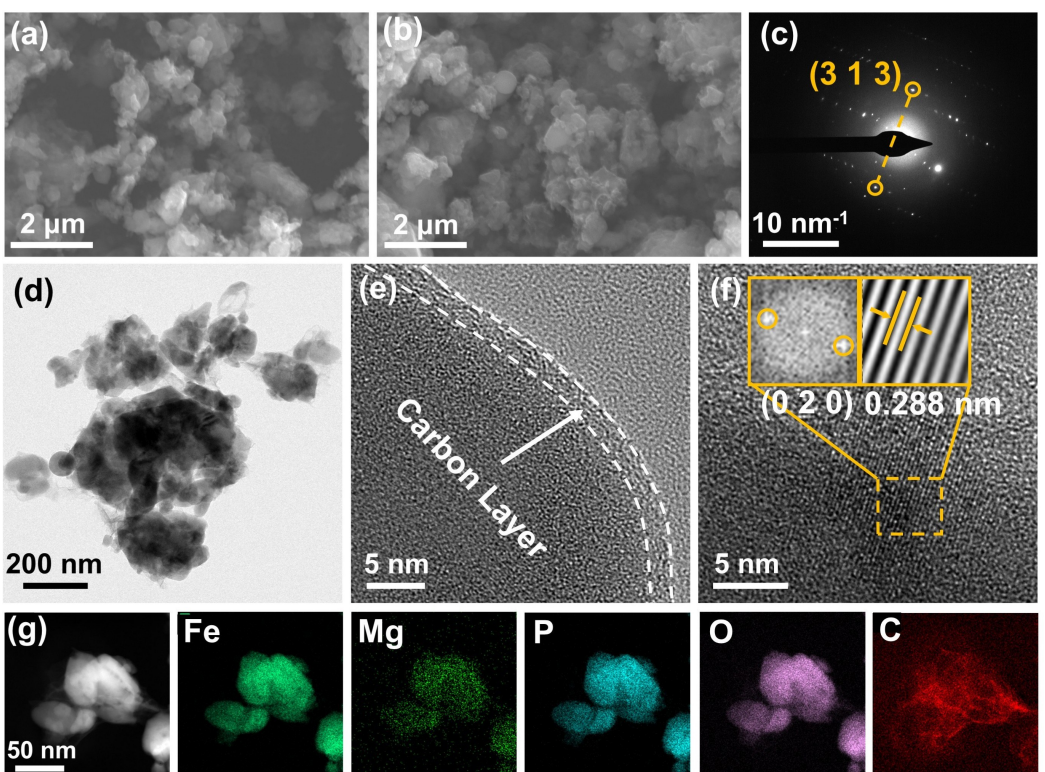


Figure 2. SEM images of (a) FP/C, (b) 0.03 Mg-FP/C. (c) SAED pattern, (d) TEM image, (e–f) HRTEM images, and (g) EDS elemental mappings of 0.03 Mg-FP/C.

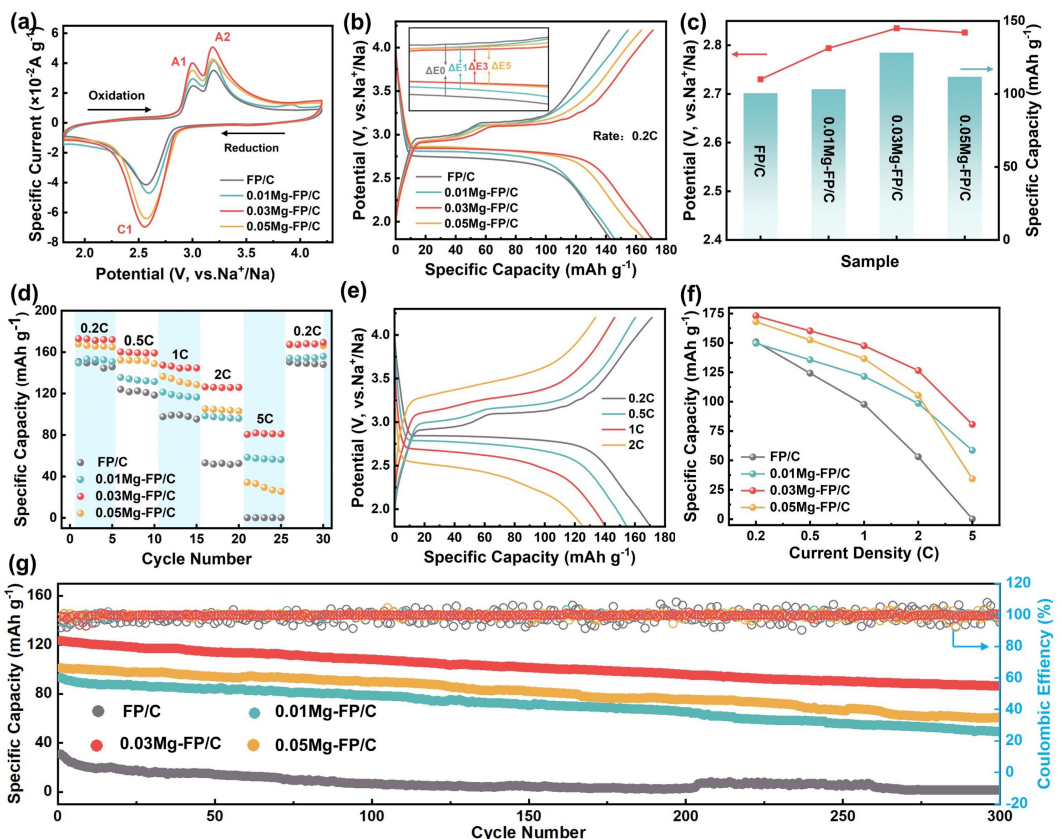


Figure 3. Electrochemical performance. (a) CV curves at a scan rate of 0.2 mV/s. (b) The GCD profiles of all samples at 0.2 C. (c) Platform voltage and platform capacity contribution of different samples. (d) Rate performance. (e) The GCD profiles of 0.03 Mg-FP/C at different C rates. (f) Discharge capacities obtained at various C-rates. (g) Cycling performance at 2 C.

exhibited a substantial voltage hysteresis of $\Delta E_0 = 0.45$ V between Na⁺ insertion and extraction, 0.03 Mg-FP/C showed a reduced potential difference of only $\Delta E_3 = 0.29$ V between charge and discharge plateaus (inset in Figure 3b). This voltage hysteresis can be attributed to the strain induced by phase transitions during NaFePO₄ desodiation and the large volume difference between NaFePO₄ and FePO₄.^[11a] The mitigated hysteresis in 0.03 Mg-FP/C is likely due to the increased lattice volume and the stabilizing influence of Mg–O bonds on the crystal structure.^[17] Subsequently, we evaluated the rate performance of all samples under varying current densities (Figure 3d, e, S4). The modified samples exhibited substantial improvements, particularly at a current density of 5 C, where 0.03 Mg-FP/C maintained a specific capacity of 80.60 mAh g⁻¹. Notably, the initial capacity and rate performance of 0.05 Mg-FP/C were suboptimal (Figure 3f), suggesting that excessive inert Mg doping adversely affects material performance. To assess the cycling stability, we conducted long-cycle tests at a current density of 2 C (Figure 3g). After 300 cycles, 0.03 Mg-FP/C retained a specific capacity of 86.39 mAh g⁻¹ with a capacity retention rate of 70.11%. In contrast, FP/C exhibited nearly zero capacity after only 250 cycles, while the capacity retention rates of 0.01 Mg-FP/C and 0.05 Mg-FP/C were 52.72% and 60.15%, respectively. These findings collectively highlight the beneficial

impact of appropriate Mg doping on enhancing the electrochemical performance of FePO₄.

The 0.03 Mg-FP/C sample exhibited exceptional Na⁺ storage capacity at high current densities, indicating a significant enhancement in Na⁺ diffusion kinetics. To elucidate this change, we conducted cyclic voltammetry (CV) and galvanostatic intermittent titration technique (GITT) tests. CV tests were performed on all samples at scan rates ranging from 0.25 to 0.4 mV s⁻¹ (Figure 4a, c, S5a, c). The data revealed a linear relationship between the peak current (I_p) and the square root of the scan rate ($v^{1/2}$), indicating the reaction was diffusion controlled^[18] (Figure 4b, d, S5b, d). Using the formula detailed in Note S1, we calculated the diffusion coefficients corresponding to the anodic and cathodic peaks, presented in Figure 4e. For the 0.03 Mg-FP/C material, the diffusion coefficients were 1.07×10^{-13} and 4.07×10^{-13} cm² s⁻¹, respectively, which are superior to those of the other samples. Figure 4f and S6 compares the GITT curves and the diffusion coefficients derived from GITT for FP/C and 0.03 Mg-FP/C (Note S2). The D_{Na^+} fluctuate around the order of 10^{-13} , consistent with the results from CV calculations. Notably, during the charging process, the diffusion coefficients in the two plateau regions are higher in the first stage and lower in the second stage. This can be attributed to the smaller volume change during the phase transition from NaFePO₄ to Na_{2/3}FePO₄ compared to the

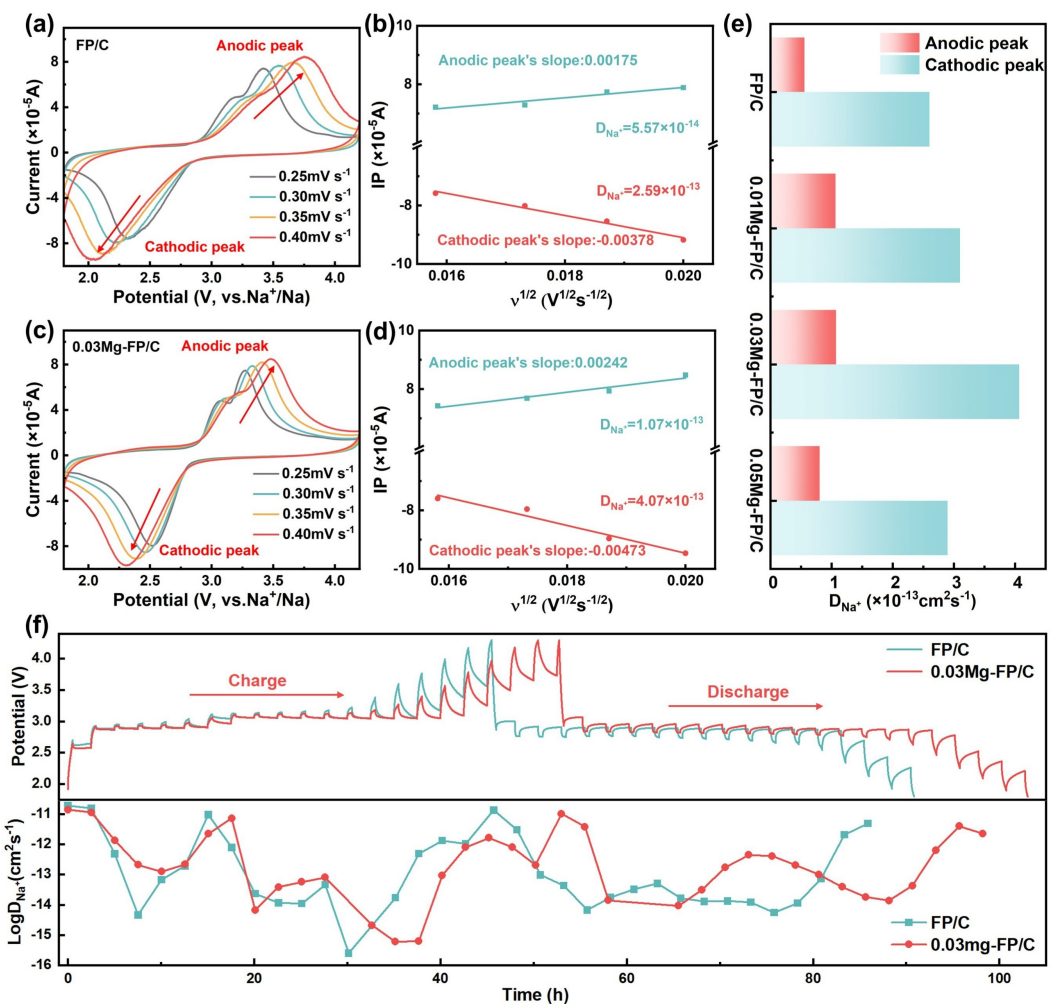


Figure 4. CV curves and the linear relationship of I_p versus $v^{1/2}$ of (a, b) FP/C and (c, d) 0.03 Mg-FP/C. (e) The Na^+ diffusion coefficient calculated from CV results. (f) GITT curves and Na^+ diffusion coefficient comparison between FP/C and 0.03 Mg-FP/C.

transition from $\text{Na}_{2/3}\text{FePO}_4$ to FePO_4 .^[9b] In both the charging and discharging plateau regions, 0.03 Mg-FP/C displays higher diffusion coefficients, this suggests that Mg doping helps to mitigate lattice volume mismatch during the charging process (Figure S7). Additionally, the stabilizing effect of Mg–O bonds further contributes to achieving rapid reaction kinetics and efficient Na^+ diffusion within the material.^[17]

Density functional theory (DFT) was employed to elucidate the effect of Mg doping on the electronic conductivity of the material. Figure 5a, b illustrate the density of states for FP/C and 0.03 Mg-FP/C. In both samples, the Fermi level intersects the energy bands, confirming their semiconducting nature. The 0.03 Mg-FP/C sample shows a higher density of states at the Fermi level, indicating an enrichment of valence electrons at the top of the valence band, which facilitates electron transitions across the bandgap to the conduction band. Mg doping substantially enhances the contribution of the p and d orbitals to the band density, and shifts the valence band closer to the Fermi level, thereby reducing the bandgap to 1.19 eV. This reduction, compared to the FP/C bandgap of 2.47 eV, indicates increased conductivity.^[19] As depicted in Figure 5c, d,

and S8, the sliced isosurface of differential charge density indicate that the distinct electron configurations of Mg and Fe result in reduced electron transfer around the MgO_6 octahedron in the 0.03 Mg-FP/C material, thereby creating a neutral region. This reduction implies decreased electrostatic repulsion from the MO_6 framework during Na^+ diffusion, which weakens the electrostatic field in the Na^+ transport channels and facilitates rapid Na^+ diffusion.^[20] Figure 5e shows the impedance test results for all materials, with 0.03 Mg-FP/C displaying the lowest charge transfer resistance (R_{ct}), which further supports its superior conductivity (Table S3). Furthermore, the Na^+ diffusion energy barrier was calculated to visually evaluate the ease of diffusion. In the one-dimensional channel along the lattice b -axis (Figure 5f), 0.03 Mg-FP/C demonstrates a lower Na^+ diffusion energy barrier. These results collectively highlight the positive effects of Mg doping on both conductivity and Na^+ diffusion.

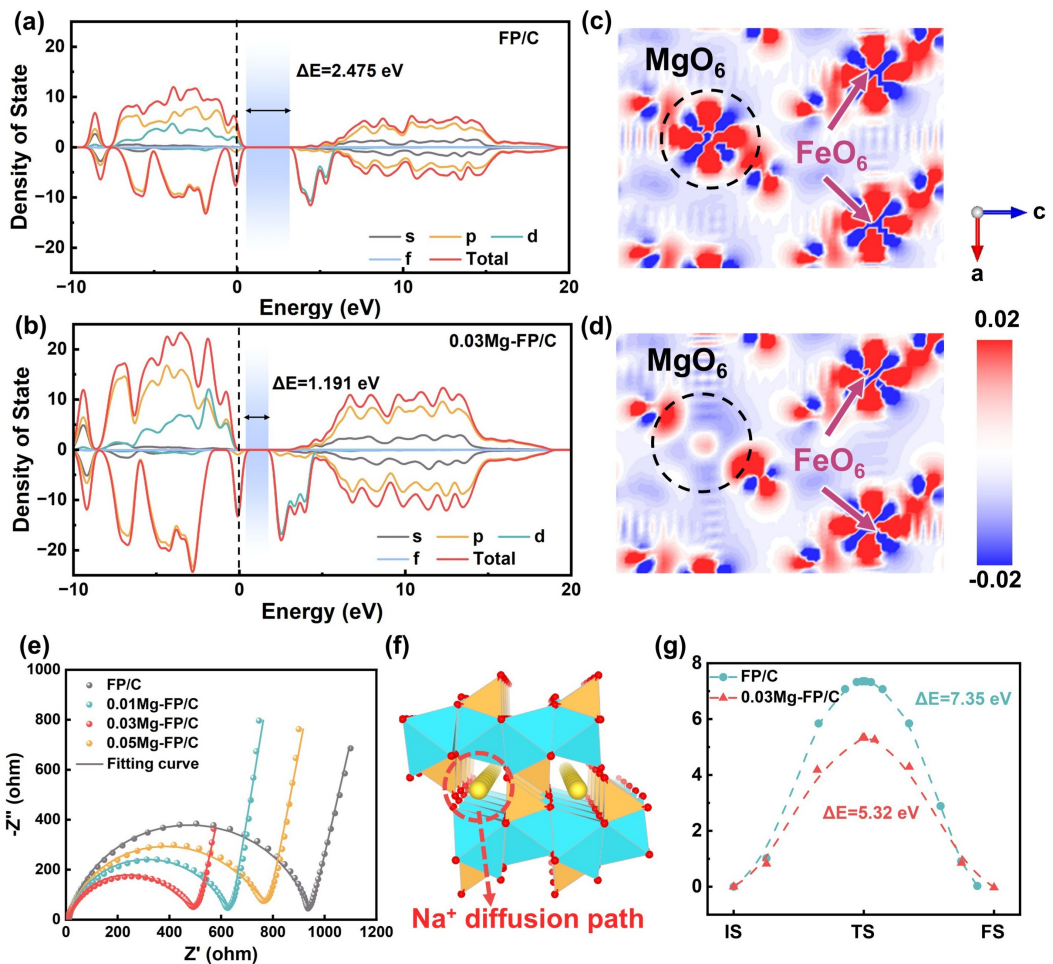


Figure 5. The density of states of (a) FP/C and (b) 0.03 Mg-FP/C. The sliced isosurface of (c) FP/C and (d) 0.03 Mg-FP/C. (e) Nyquist plots. (f) Na^+ Diffusion pathway and (g) Migration energy barrier of Na^+ along this pathway.

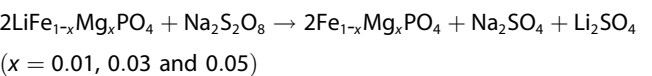
Conclusions

In conclusion, this study synthesized Mg-doped olivine-type FePO_4 using an aqueous ion exchange method. Rietveld refinements and kinetic analyses indicate that the doped sample possesses wider Na^+ diffusion channels and enhanced Na^+ diffusion kinetics. Moreover, due to the volumetric changes induced by doping and the stabilizing effect of the Mg–O bond on the lattice, 0.03 Mg-FP/C demonstrates minimal voltage hysteresis during constant current charge-discharge tests. Density of states and differential charge density analyses provide a microscopic explanation for the improvements in conductivity and Na^+ diffusion kinetics in the modified material. Ultimately, 0.03 Mg-FP/C exhibits excellent electrochemical performance, achieving $170.54 \text{ mAh g}^{-1}$ at 0.2 C and 80.60 mAh g^{-1} at 5 C, with a capacity retention of 70.11% after 300 cycles at 2 C. This research enhances the Na^+ storage performance of FePO_4 by mitigating voltage hysteresis, offering a novel reference solution for lithium resource recycling and the development of future Na^+ battery cathodes.

Experimental Section

Material Synthesis

$\text{Fe}_{1-x}\text{Mg}_x\text{PO}_4/\text{C}$ composites with varying Mg^{2+} content ($x=0$ for FP/C; $x=0.01$ for 0.01 Mg-FP/C; $x=0.03$ for 0.03 Mg-FP/C; $x=0.05$ for 0.05 Mg-FP/C) were synthesized using $\text{LiFe}_{1-x}\text{Mg}_x\text{PO}_4$ in an aqueous solution through ion exchange. The synthesis comprised two main steps. (1) Preparation of $\text{LiFe}_{1-x}\text{Mg}_x\text{PO}_4$: Stoichiometric quantities of Li_2CO_3 , $\text{FePO}_4 \cdot 2\text{H}_2\text{O}$, $\text{Mg}(\text{CH}_3\text{COO})_2$, and $\text{C}_6\text{H}_8\text{O}_7$ were combined in a ball mill and ground at 400 rpm for 4 hours to create the precursor. This precursor was subsequently calcined in a tube furnace at 700°C for 12 h under an argon atmosphere. (2) Delithiation: The $\text{LiFe}_{1-x}\text{Mg}_x\text{PO}_4$ obtained from step (1) was evenly dispersed in an 0.1 mol/L aqueous $\text{Na}_2\text{S}_2\text{O}_8$ solution and stirred at 25°C for 24 h, undergoing the following chemical reaction to produce $\text{Fe}_{1-x}\text{Mg}_x\text{PO}_4/\text{C}$:



Material Characterization

The crystal structure of the samples was characterized using an Ultima VI X-ray diffractometer (Rigaku, Japan) with Cu $\text{K}\alpha$ radiation, scanning over a range of 5° to 90°. The carbon content was measured using a high-frequency infrared carbon-sulfur analyzer (SCIENCE HCS-801). Scanning Electron Microscopy (SEM, Hitachi SU-5000), Transmission Electron Microscopy (TEM, Hitachi HT770), and High-Resolution Transmission Electron Microscopy (HRTEM, Talos F200X G2) were utilized to assess the size, morphology, lattice fringes, selected area electron diffraction patterns, and energy-dispersive spectroscopy of the materials. The valence states of the elements were analyzed using X-ray photoelectron spectroscopy (ESCALAB 250XI).

Electrochemical Measurements

The active material powder, conductive carbon black, and binder were thoroughly mixed in a mass ratio of 8:1:1 using a mortar. The mixture was combined with NMP as a solvent to create a slurry, which was uniformly coated onto aluminum foil and dried overnight in an oven at 110°C. The aforementioned aluminum foil was cut into disks with a diameter of 12 mm to serve as the positive electrode, while a metallic sodium sheet served as the negative electrode. A Whatman glass fiber membrane (GF/A) was employed as the separator, and 1 M NaClO_4 dissolved in a mixed solvent (with a volume ratio of DEC/EC/DMC = 1:1:1 and 5% FEC) was used as the electrolyte. The coin cells (CR2025) were assembled in a glove box filled with high-purity argon gas. Constant current charge-discharge tests and galvanostatic intermittent titration technique tests were conducted on the half-cells within a voltage range of 1.8–4.2 V (NEWARE test system). Electrochemical impedance spectroscopy and cyclic voltammetry tests were performed using a CHI660D electrochemical workstation (Shanghai Chenhua).

Acknowledgements

This work was supported by the National Natural Science Foundation of China (51974190; 52474331).

Conflict of Interests

The authors declare no conflict of interest.

Data Availability Statement

The data that support the findings of this study are available from the corresponding author upon reasonable request.

Keywords: Sodium ion batteries • Olivine- FePO_4 • Cathode materials • Doping • Voltage hysteresis

- [1] a) D. Larcher, J. M. Tarascon, *Nat. Chem.* **2015**, *7*, 19; b) E. Hossain, H. M. R. Faruque, M. S. H. Sunny, N. Mohammad, N. Nawar, *Energies* **2020**, *13*, 3651.
- [2] a) E. Bullich-Massagué, F. J. Cifuentes-García, I. Glenny-Crende, M. Cheah-Mañé, M. Aragüés-Peñalba, F. Díaz-González, O. Gomis-Bellmunt,

Appl. Energy **2020**, *274*, 115213; b) S. Chu, A. Majumdar, *Nature* **2012**, *488*, 294.

- [3] a) A. Manthiram, *ACS Cent. Sci.* **2017**, *3*, 1063; b) W. H. Zuo, R. Z. Li, C. Zhou, Y. Y. Li, J. L. Xia, J. P. Liu, *Adv. Sci.* **2017**, *4*, 1600539.
- [4] A. K. Padhi, K. S. Nanjundaswamy, J. B. Goodenough, *J. Electrochem. Soc.* **1997**, *144*, 1188.
- [5] a) H. Liu, X. X. Liu, W. Li, X. Guo, Y. Wang, G. X. Wang, D. Y. Zhao, *Adv. Energy Mater.* **2017**, *7*, 1700283; b) S. E. Kesler, P. W. Gruber, P. A. Medina, G. A. Keeleian, M. P. Everson, T. J. Wallington, *Ore Geol. Rev.* **2012**, *48*, 55.
- [6] a) N. Yabuuchi, K. Kubota, M. Dahbi, S. Komaba, *Chem. Rev.* **2014**, *114*, 11636; b) S. Y. Hong, Y. Kim, Y. Park, A. Choi, N. S. Choi, K. T. Lee, *Energy Environ. Sci.* **2013**, *6*, 2067; c) H. J. Liang, H. H. Liu, J. Z. Guo, X. X. Zhao, Z. Y. Gu, J. L. Yang, X. Y. Zhang, Z. M. Liu, W. L. Li, X. L. Wu, *Ener. Storage Mater.* **2024**, *66*, 103230; d) J. L. Yang, X. X. Zhao, W. Zhang, K. Ren, X. X. Luo, J. M. Cao, S. H. Zheng, W. L. Li, X. L. Wu, *Angew. Chem. Int. Ed.* **2023**, *62*, e202300258.
- [7] a) W. B. Fei, X. P. Zhang, K. Y. Sun, Y. Wang, K. X. Rao, M. T. Deng, C. D. Tao, L. Wu, Y. L. Sui, *Ener. Storage Mater.* **2024**, *73*, 103848; b) S. X. Lu, J. X. Zhang, M. T. Deng, K. X. Rao, Y. Wang, K. Y. Sun, W. B. Fei, X. P. Zhang, M. Y. Xiao, L. Wu, Y. L. Sui, *Appl. Surf. Sci.* **2024**, *665*, 160350; c) M. T. Deng, Y. L. Sui, K. X. Rao, Y. Wang, W. B. Fei, K. Y. Sun, Z. L. Yang, X. P. Zhang, L. Wu, *Chem. Eng. J.* **2024**, *499*, 156347; d) C. Z. Ma, J. Alvarado, J. Xu, R. J. Clément, M. Kodur, W. Tong, C. P. Grey, Y. S. Meng, *J. Am. Chem. Soc.* **2017**, *139*, 4835; e) X. X. Zhao, X. T. Wang, Z. Y. Gu, J. Z. Guo, J. M. Cao, Y. Liu, J. Li, Z. X. Huang, J. P. Zhang, X. L. Wu, *Adv. Funct. Mater.* **2024**, *34*, 2402447.
- [8] a) Y. Wang, W. B. Fei, X. P. Zhang, M. T. Deng, S. X. Lu, J. X. Zhang, K. X. Rao, Y. Yuan, Y. L. Sui, L. Wu, *J. Colloid Interface Sci.* **2024**, *664*, 220; b) W. B. Fei, Y. Wang, X. P. Zhang, J. X. Zhang, S. X. Lu, K. X. Rao, K. Y. Sun, M. T. Deng, Y. X. Liu, Q. Q. Li, L. Wu, Y. L. Sui, *Chem. Eng. J.* **2024**, *493*, 152523.
- [9] a) P. Moreau, D. Guyomard, J. Gaubicher, F. Boucher, *Chem. Mater.* **2010**, *22*, 4126; b) M. Casas-Cabanas, V. V. Roddatis, D. Saurel, P. Kubiak, J. Carretero-González, V. Palomares, P. Serras, T. Rojo, *J. Mater. Chem.* **2012**, *22*, 17421.
- [10] a) Y. J. Fang, Q. Liu, L. F. Xiao, X. P. Ai, H. X. Yang, Y. L. Cao, *ACS Appl. Mater. Interfaces* **2015**, *7*, 17977; b) N. Wongitharom, C. H. Wang, Y. C. Wang, C. H. Yang, J. K. Chang, *ACS Appl. Mater. Interfaces* **2014**, *6*, 17564; c) T. T. Gan, J. S. Yuan, F. Chen, G. D. Zhang, L. H. Liu, L. Zhou, Y. F. Gao, Y. G. Xia, *Small* **2024**, *20*, 2401489; d) Y. Y. Xu, R. Dai, X. J. Wang, Z. J. Qiao, H. W. Wen, D. B. Ruan, Y. Z. Wang, *Chem. Phys. Lett.* **2024**, *834*, 140983; e) F. Nozaki, S. Shomura, J. Hwang, K. Matsumoto, R. Hagiwara, *ACS Sustain. Chem. Eng.* **2023**, *11*, 1037.
- [11] a) Y. J. Zhu, Y. H. Xu, Y. H. Liu, C. Luo, C. S. Wang, *Nanoscale* **2013**, *5*, 780; b) M. Galceran, D. Saurel, B. Acebedo, V. V. Roddatis, E. Martin, T. Rojo, M. Casas-Cabanas, *Phys. Chem. Chem. Phys.* **2014**, *16*, 8837.
- [12] a) D. Saurel, M. Giner, M. Galceran, J. Rodriguez-Carvajal, M. Reynaud, M. Casas-Cabanas, *Electrochim. Acta* **2022**, *425*, 140650; b) C. Henriksen, J. K. Mathiesen, Y. M. Chiang, K. M. O. Jensen, D. B. Ravnsbæk, *ACS Appl. Energy Mater.* **2019**, *2*, 8060.
- [13] a) C. Berlanga, I. Monterrubio, M. Armand, T. Rojo, M. Galceran, M. Casas-Cabanas, *ACS Sustain. Chem. Eng.* **2020**, *8*, 725; b) S. H. Zeng, Q. X. Xu, H. J. Jin, L. X. Zeng, Y. Y. Wang, W. B. Lai, Q. Yao, J. X. Zhang, Q. H. Chen, Q. R. Qian, *J. Electroanal. Chem.* **2022**, *913*, 116287.
- [14] a) H. Zhang, Y. H. Tang, J. Q. Shen, X. G. Xin, L. X. Cui, L. J. Chen, C. Y. Ouyang, S. Q. Shi, L. Q. Chen, *Appl. Phys. A-Mater.* **2011**, *104*, 529; b) M. Nakayama, S. Yamada, R. Jalem, T. Kasuga, *Solid State Ion.* **2016**, *286*, 40.
- [15] Y. Y. Liu, C. K. Chang, J. N. Zheng, *J. Storage Mater.* **2024**, *91*, 112108.
- [16] S. Guo, M. D. Liu, L. M. You, G. Cheng, J. Li, K. Zhou, *Chemosphere* **2021**, *279*, 130482.
- [17] J. Li, X. D. Zhao, P. G. He, Y. K. Liu, J. T. Jin, Q. Y. Shen, Y. Wang, S. W. Li, X. H. Qu, Y. C. Liu, L. F. Jiao, *Small* **2022**, *18*, 2202879.
- [18] X. J. Pu, D. Zhao, C. L. Fu, Z. X. Chen, S. N. Cao, C. S. Wang, Y. L. Cao, *Angew. Chem. Int. Ed.* **2021**, *60*, 21310.
- [19] Q. He, B. Yu, Z. H. Li, Y. Zhao, *Energy Environ. Mater.* **2019**, *2*, 264.
- [20] J. J. Wang, H. B. Jing, X. M. Wang, Y. Q. Xue, Q. H. Liang, W. H. Qi, H. Yu, C. F. Du, *Adv. Funct. Mater.* **2024**, *34*, 2315318.

Manuscript received: January 18, 2025

Revised manuscript received: February 14, 2025

Accepted manuscript online: February 25, 2025

Version of record online: March 12, 2025